Comparison of calibration strategies for a high sensitivity PEI-based RF humidity sensor

Bernard Bobby Ngoune, Marine Dumon, Balakumara Vignesh, Benoit Bondu, Senthilmurugan Subbiah, Guillaume Perrin, Stéphane Bila, Corinne Dejous, Berengère Lebental, Hamida Hallil

Comparison of calibration strategies for a high sensitivity RF humidity sensor

Bernard Bobby Ngoune, Marine Dumon, Balakumara Vignesh, Benoit Bondu, Senthilmurugan Subbiah, Guillaume Perrin, Stéphane Bila, Corinne Dejous, Berengère Lebental, and Hamida Hallil

***Abstract*—In this study, a radio frequency (RF) humidity sensor for monitoring outdoor relative humidity (RH) was developed using polyethyleneimine as sensing material. The sensor's performance was assessed in laboratory and outdoor conditions. The primary sensor demonstrated an exponential sensitivity in frequency and magnitude, approximately -3.65 MHz/%RH and -7.69 MHz/%RH, -0.051 dB/%RH and -0.12 dB/%RH, across the RH ranges of 30 – 50 %RH and 50 – 70 %RH respectively, with consistent results from 25 °C to 45 °C. The sensor exhibited a rapid response and recovery time of 22 s/44 s, with minimal hysteresis and marginal cross-sensitivity to temperature. Following calibration using different calibration methods (analytical and machine-learning-based techniques), the RH prediction performance was gauged on a separate dataset. The exponential calibration law achieved mean absolute errors (MAE) as low as 0.8 %RH, while other methods like Gaussian Regression Process, k-nearest neighbour (KNN), and generalized linear regression (GLR) resulted in MAE of 0.9 %RH, 1 %RH, and 1.1 %RH. A secondary sensor, also exhibiting exponential sensitivity, underwent initial laboratory testing before transitioning to outdoor conditions. Applying laboratory calibration to outdoor data resulted in a MAE of 4.4%RH, showing remarkable transferability with only 0.8%RH increased MAE. Cross-sensitivity analysis revealed no dependency with temperature, NO_2, NO, CO, CO_2, and O_3 in outdoor conditions. Finally, we confirmed the transferability of calibration between the two sensors under laboratory and outdoor conditions, utilizing output standardization with the slope-bias correction algorithm. This research underscores the potential of our RF humidity sensor for accurate outdoor RH monitoring.**

***Index Terms*—Radiofrequency sensor, microwave, humidity, calibration, machine learning, polymer sensing material**

I. Introduction

RECENTLY, there has been a considerable increase in the utilization of RF sensors, combined with various sensing materials, for gas detection and humidity measurement applications [1, 2]. This growth is largely attributable to their efficient energy consumption, cost-effectiveness, durability, and high operational frequency that enables wireless data transmission [3, 4]. These attributes are essential for tracking relative humidity (RH), a crucial variable consistently scrutinized across diverse sectors such as atmospheric sciences, food industry, agriculture, and healthcare [5, 6]. For these applications, desired sensor properties include high sensitivity, rapid response and recovery times, minimal drift, reversibility, repeatability, and low hysteresis [7, 8]. RF sensors are frequently paired with sensitive polymers for humidity monitoring due to the polymers high sensitivity, adaptability, and easy functionalization [9]. Typically, the sensors described in the literature are calibrated under laboratory conditions, which allows for the identification of their unique dependencies on parameters such as RH, temperature, or environmental gases [10]. Calibration involves the construction of parametric models that relate sensor responses to different variables of interest. This can be accomplished either through the direct identification of the coefficients of an analytical model [11], or by machine learning (ML) methods such as linear regression (LR), generalized linear regression (GLR), support vector machine regression (SVM), Gaussian process regression (GPR), Random Forest (RF), and k-nearest neighbours (KNN). LR

This paper was submitted for review on 31 May 2023.

B. Ngoune, C. Dejous, and H. Hallil are with Univ. Bordeaux, CNRS, IMS, UMR 5218, Bordeaux INP, F-33405 Talence, France (e-mails: bernard-bobby.ngoune@u-bordeaux.fr, corinne.dejous@u-bordeaux.fr, and hamida.hallil-abbas@u-bordeaux.fr).

M. Dumon, G. Perrin, B. Vignesh, and B. Lebental are with COSYS-IMSE, Université Gustave Eiffel, F-77420 Marne-La-Vallée, France (e-mails: marine.dumon@univ-eiffel.fr, guillaume.perrin@univ-eiffel.fr, balakumara.vignesh@univ-eiffel.fr and berengere.lebental@univ-eiffel.fr).

B. Bondu is with ISORG, 17 rue Soyouz, Parc ESTER Technopole, 87068 Limoges, France (e-mail: benoit.bondu@isorg.fr).

Stéphane Bila is with University of Limoges, CNRS, XLIM UMR 7252, F-87060 Limoges, France (email: stephane.bila@xlim.fr)

B.Vignesh and S. Subbiah are with Water and Energy Nexus Laboratory, Department of Chemical Engineering, Indian Institute of Technology Guwahati, India (e-mail : senthilmurugan@iitg.ac.in).

constructs a linear equation to describe the relationship between sensor responses and reference measurements [12]. GLR extends this approach by employing a polynomial function to model the same relationship [13]. In such cases, the polynomial order functions as a tunable hyperparameter to approximate the actual relationship as closely as possible. SVM serves as a ML regressor that identifies an optimal hyperplane to categorize sensor data. This nonparametric method is contingent on kernel functions like linear, polynomial, and radial basis function (RBF), with the RBF kernel being widely used for modeling non-linear relationships between sensor response and reference measurement [14]. The Random Forest regressor is an ensemble of decision tree

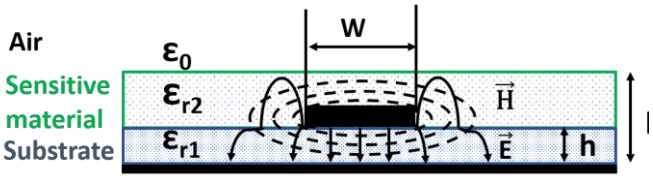

Fig. 1. Multilayer microstrip line with sensing layer deposited on the substrate.

regressors, amalgamated using a bagging technique [15]. These decision trees operate as concurrent estimators, improving accuracy and mitigating overfitting, although this also results in longer prediction times. KNN model memorizes the training data and predicts new data values based on their proximity to known values [16]. The predicted value for a new data point is obtained using $y_{new}(x_{new}) = \frac{1}{k} \sum_{i \in k(x_{new})} y_i$, where $k(x_{new})$ is the set of k nearest neighbours of x_{new}. GPR is yet another ML regressor that posits the function to be predicted as a specific instance of a Gaussian process, with the mean and covariance functions derived from the data [13]. Among these models, simpler and more explicit ones, such as GLR and SVM Regression, are especially suitable for sensor calibration based on laboratory data due to their modest data needs [17, 18].

Regardless of the chosen model, the transferability of calibration models from laboratory settings to field conditions and across different sensors remains a significant challenge in the literature. When used in field conditions, uncontrollable environmental parameters such as temperature and other gases often degrade performance, thereby limiting the practical implementation of the sensors in industrial scenarios [19]. Additionally, variability between sensors typically precludes the direct application of the same model across different sensors, necessitating comprehensive recalibration of each individual sensor, which results in prohibitive sensor costs. Strategies such as direct calibration in field conditions, as developed on the Sense-City platform, and the use of calibration transfer algorithms, offer promising solutions to enhance the viability of cost-effective sensors for environmental applications [8].

This paper evaluates the performance of a highly sensitive, flexible RF polymer-based relative humidity sensor for outdoor applications, using various calibration methodologies. The sensor is designed with two interdigitated resonators, one of which is coated with a thin polyethyleneimine layer serving as the humidity-sensing material (Section II). The responses of two distinct sensors were assessed in laboratory (Section III) and outdoor conditions (Section IV), and different calibration algorithms were compared across the various datasets, including calibration transfer (Section V).

II. MATERIALS AND METHODS

A. Interdigitated microstrip resonator as transducer

The transducer of choice is a multilayer microstrip resonator. As depicted in Fig.1, this microstrip line's cross-section comprises multiple layers of varying dielectric materials, each with a distinct relative permittivity (ε_r). The top layer, constituting of the sensing material, is designed to be highly sensitive to a specific target species, in this case, humidity.

Given a microstrip of width (w), a substrate with relative permittivity ε_{r1} and height h, a sensing layer with relative permittivity ε_{r2} and height h_2-h, and an air layer with permittivity ε_0, the effective permittivity (ε_{eff}) of the multilayer microstrip line is determined via the conformal mapping method detailed in the study of J. Svacina [20]. This is expressed by the equation:

$$\varepsilon_{eff} = \varepsilon_{r1} q_1 + \varepsilon_{r2} \frac{(1 - q_1)^2}{\varepsilon_{r2}(1 - q_1 - q_2) + q_2} \quad (1)$$

where q_1 and q_2 are the filling factors for the line as defined in [21]. The filling factor q_2 diminishes as the sensing layer thickness (h_2 - h) grows, leading to an increase in ε_{eff}. The sensing principle depends on the sensing material's dielectric properties changing with the presence of the target species, causing a shift in the effective permittivity ε_{eff}. This shift prompts a variation in resonance frequency, phase, and magnitude [22]. The resonance frequency is inversely proportional to ε_{eff}, as per the equation:

$$f_{res} = \frac{c}{\lambda_r \sqrt{\varepsilon_{eff}}} \quad (2)$$

where f_{res} is the resonance frequency, c is the wave speed, and λ_r is the wavelength of the microstrip line. Its reflection coefficient also heavily depends on ε_{eff}, as well as the line conductor's properties (conductivity) and dimensions (length and width). These ε_{eff} variations are monitored by measuring the resonator's scattering parameters, reflection S_{11} and transmission S_{21} coefficients using a vector network analyzer (VNA).

B. Humidity sensor design and fabrication

The humidity sensor design is depicted in Fig. 2a. It comprises two-channel interdigitated resonators constructed from 18 µm thick by 180 µm wide copper lines with gold nickel plating, printed on a flexible Kapton substrate. One channel is kept bare (reference channel), while the other is coated with the desired sensing material (sensitive channel). The reference channel was designed to resonate at 3.28 GHz and simulated using the ANSYS HFSS™ finite element method (FEM) tool. A differential configuration was employed to minimize variations unrelated to the sensing material. The interdigitated resonator design based on resonant finger coupling was selected as it enhances the electric field density on the surface, facilitating interaction with the target species. An augmentation in the thickness of the sensitive layer results in a reduction of the resonance frequency and an

enhancement in sensitivity to dielectric variations of the sensitive material. Additionally, an increase in layer thickness may lead to prolonged sensor response and recovery times [23]. Consequently, a meticulous equilibrium was established to optimize sensitivity while minimizing response and recovery times during the selection of the sensitive layer thickness.

The designed transducer was fabricated by Würth electronics [24]. A double-sided copper-clad Kapton laminate from DuPont™ Pyralux® AP, 100 µm thick, was used as the substrate [25]. This material is ideal for multilayer flex and rigid-flex applications, demonstrating high hydrophobicity and excellent thermal resistance. To prevent oxidation, the copper-clad substrate was treated with an immersion coating of electroless nickel and gold.

The chosen sensing material was commercially available polyethyleneimine (PEI) 25 kDa, procured from Polysciences Inc. This selection was due to its adaptability and its extremely low water contact angle (<5°), which allows high permittivity water molecules (ε_r = 80) to readily adhere to the polymer, subsequently altering the ε_{eff} of the PEI layer. A small quantity of PEI powder was dissolved in chloroform (Fischer Scientific, reference C/4960/17, purity 99.8+%) at a concentration of 150 mg/ml, achieved through magnetic stirring at room temperature. This solution was then applied on the sensitive resonator area via spin coating at 2000 rpm for 30 seconds, while the reference resonator was protected with adhesive tape. The coating was followed by an overnight baking process in a nitrogen oven at 100 °C, then the adhesive tape was removed. The resulting layer thickness on the active area was approximated to be 1.2 µm, as measured by profilometry (DektakXT, Bruker). Fig. 2b illustrates the resultant sensor with a thickness of 1.2 µm.

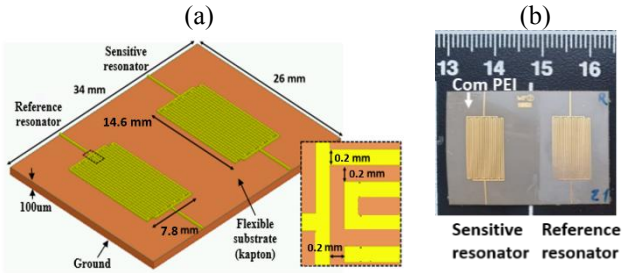

Fig. 2. (a) Sensor design and (b) the fabricated sensor coated with Com PEI.

C. Laboratory and outdoor experimental setups

The sensor was characterized through two distinct experimental setups initially under controlled laboratory conditions, followed by outdoor testing. The laboratory arrangement comprised of a climatic chamber (CLIMAT EXCAL2) for generating varying humidity levels (25 – 90 %RH) under a controlled temperature, a 4 PORT VNA (Keysight E5080a) for assessing the S_{ij} parameters, a benchmark temperature and humidity sensor (SHT85), an Arduino UNO, and a Raspberry Pi 4 for overseeing instrument control and data collection. The SHT85 sensor was linked to the Arduino UNO, which was then connected to the Raspberry Pi 4 via USB. Additionally, a calibration gas generator (OWLSTONE, OHG) was deployed to create humidity within the 0-90 %RH range. The resonance frequency and magnitude were derived from the reflection S_{11} parameter employing the algorithm outlined in [8]. Differential measurements were procured by subtracting the responses of the coated resonators' frequency and magnitude from those of the uncoated resonators, aiming to mitigate effects associated with substrate properties.

Outdoor experiments were conducted at the Sense-City large-scale facility, a platform encompassing primary components of urban ecosystems such as roads, buildings, subterranean networks, lighting, and vegetation. Monitoring of pollutant gas concentrations was accomplished by environmental analyzers (Envea AC32e for NO and NO_2, Envea O342e for O_3, Envea CO12e for CO and CO_2), while the Vaisala WXT536 weather station tracked temperature and humidity. In Sense-City, the microstrip sensors were connected to a two-port VNA (Anritsu MS2724B) via coaxial wires for S_{ij} parameters measurement. This setup was further linked to a Raspberry Pi 4 for continuous instrument control, data collection, and processing. The VNA and Raspberry Pi were kept indoors, whereas the sensor was housed in a test cell and installed outdoors on the side of the Sense-City climate chamber near the inlet tubes of the environmental analyzers, as illustrated in Fig.3.

.

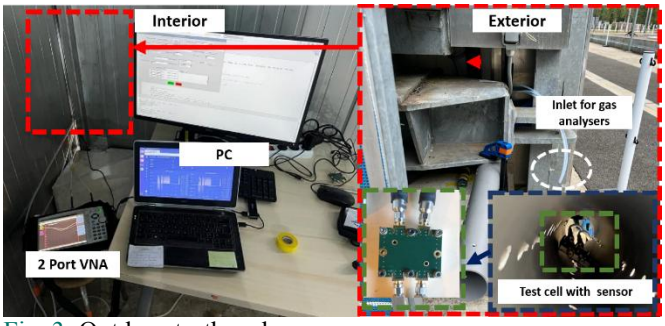

Fig. 3. Outdoor testbench

D. Calibration models

The calibration models all utilize the sensor's differential frequency and magnitude responses as inputs (freqdiff and magdiff). To denoise and smooth the raw data, both median and Gaussian filters are applied. The data undergo normalization using the standard scaler function from the sklearn library [26]. The specifics for training, testing, and validation datasets are detailed in their respective sections.

To evaluate performance, commonly used indicators are employed: coefficient of determination (R^2), mean absolute error (MAE), and mean absolute percentage error (MAPE) [27]. Additionally, computation times are estimated using two different computers. Computer X (Intel(R) Core (TM) i5-10210U CPU @ 1.60GHz, 2.11 GHz 16 GB RAM) is used for analytical models, linear regression (LR), random forest (RF), support vector machine (SVM), and k-nearest neighbors (KNN), while computer Y (11th Gen Intel(R) Core (TM) i7-1185G7 @ 3.00GHz 3.00 GHz 32,0 Go RAM) is utilized for Gaussian process regression (GPR) and generalized linear regression (GLR).

III. LABORATORY CHARACTERIZATION

A. *Electrical characterisation of the resonator*

An uncoated resonator was electrically characterized for S_{ij} parameters (S_{11} and S_{21}) using a VNA, with the results compared to simulations as shown in Fig. 4a. The measured S_{ij} parameters aligned well with the simulation results, and any minor discrepancies were attributed to slight variations in substrate and conductor properties. When the sensitive polymer was deposited, an expected increase in ε_{eff} was observed, leading to a corresponding decrease in resonance frequency, as seen in Fig. 4b.

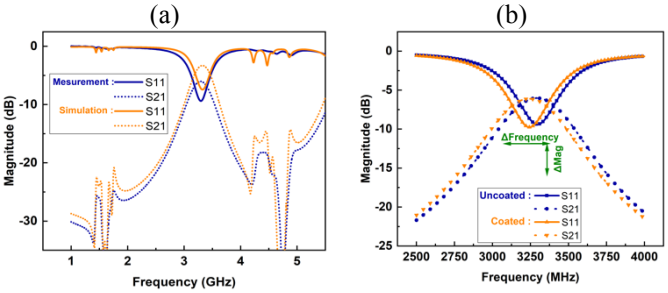

Fig. 4. (a) Comparison of simulated and measured S_{ij} parameters for the bare resonator (b) Measured S_{ij} parameters for the uncoated and PEI-coated resonators

B. *Dynamic response to RH at various temperatures*

Sensor S1 was characterized under varying humidity levels ranging from 25 to 70 %RH at different temperatures (25 – 45 °C). Two sets of 22-hour experiments were conducted: the first one (labelled E1) to determine the sensor's sensing characteristics and calibrate it, and the second one (labelled E2) to test the calibration models constructed on an unseen dataset.

The differential resonance frequency during exposure to six RH cycles at different temperatures (25 °C, 30 °C, 30 °C, 35 °C, 40 °C, 45 °C) is displayed as a green line in Fig. 5a, alongside the RH (grey line) measured by the benchmark sensor (SHT85). Figs. 5b and 5c focus on the second 30°C cycle, presenting the resonance frequency and magnitude.

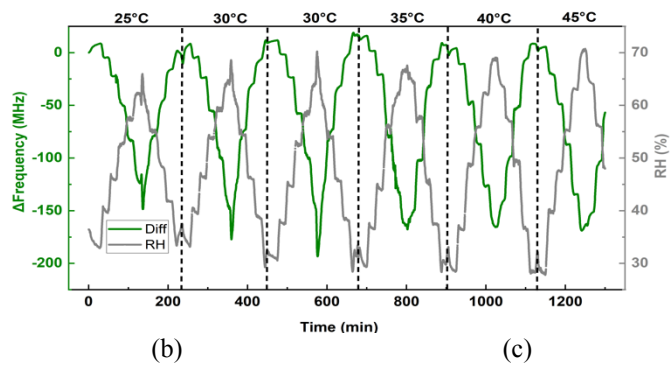

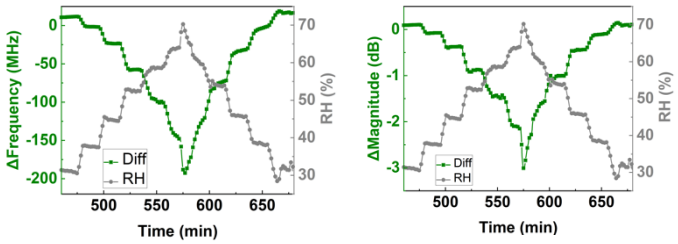

Fig. 5. (a) Differential frequency response to variations in RH at different temperatures, and the detailed differential frequency response (b) and magnitude response (c) to RH at 30 °C. The green lines represent the sensor responses and the grey lines the relative humidity measured by the benchmark sensor SHT85.

As the RH increases, the resonance frequency and its magnitude decrease due to the PEI's water molecule sorption, which results in an increase in ε_{eff}. The temperature's impact on the response appears to be insignificant, which will be confirmed in the next part.

C. *Sensitivity and analytical calibration relationship*

The sensor's RH sensing characteristics are derived from scatter plots of frequency versus RH (Δf) and magnitude (ΔMag) versus RH as shown in Figs. 6a and 6b (for frequency and magnitude responses, respectively).

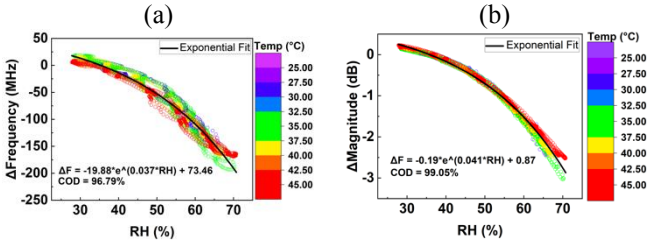

Fig. 6. Calibration curve illustrating the sensor's frequency (a) and magnitude (b) response to RH at various temperatures, with the black line representing an exponential fit.

Both parameters exhibit an exponential response to RH (linear in a log-lin plot) over the entire range (25 – 70 %RH), and this response is independent of temperature. After applying a median and Gaussian filter to denoise and smooth the raw data, the analytical calibration relationships are identified as:

$$\Delta f\ (\text{MHz}) = -20 * e^{(0.037*\text{RH})} + 74 \quad (3)$$

$$\Delta\text{Mag}\ (\text{dB}) = -0.19 * e^{(0.041*\text{RH})} + 0.87 \quad (4)$$

For comparison with existing research, the exponential calibration relationships are approximated by piece-wise linear relationships, yielding sensitivities of -3.7 MHz/%RH and -0.051 dB/%RH over the range 30 – 50 %RH, and -7.7 MHz/%RH and -0.12 dB/%RH over the range 50 – 70 %RH.

The sensor also displays low hysteresis H (<5% and <1% in frequency and magnitude, respectively), as calculated by the formula:

$$\text{H}\ (\%) = \frac{\Delta max\ \delta}{\delta_{max} - \delta_{min}} \quad (5)$$

where δ_{max} and δ_{min} are the maximum and minimum value for the sensor response δ and Δmax δ is the maximum difference in the sensor response absorption and desorption cycle.

The standard deviation of the frequency and magnitude response in the 30 – 50 %RH range is 21 MHz and 0.28 dB, respectively. This yields a limit of detection (LOD) of 19

%RH in either case, with the LOD defined in the standard manner [28] by LOD = $\frac{3.3*\sigma}{S}$ where σ is the standard deviation of the response and S is the sensitivity.

D. *Response and recovery times*

Figs. 7a and 7b illustrate the sensor's differential frequency response when relative humidity is increased (from 60 to 72 %RH) and decreased (from 86 downto 1.5 %RH) at ambient temperature (22 °C).

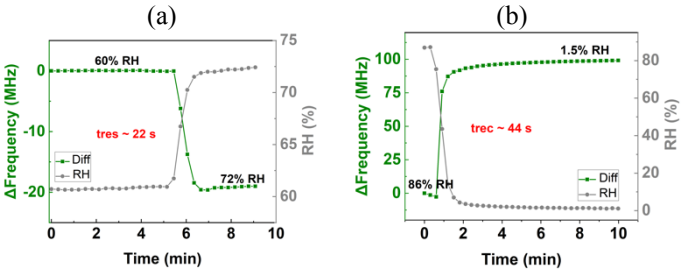

Fig. 7. Differential frequency response to (a) increasing and (b) decreasing steps of RH at ambient temperature (22 °C) along with the corresponding response and recovery times.

The sensor's response and recovery time are determined by measuring the duration required to reach 90% of the maximal response change for RH absorption and desorption, respectively. At 22 °C, the sensor demonstrates a response/recovery time of 22 s/44 s, respectively, which is slightly longer than that of the SHT85 sensor (10 s).

E. *ML-based calibration and RH prediction*

The performance of a calibration based on the exponential relationships described in section III. C is compared with that of six additional methods: LR, GLR, SVM, GPR, Random Forest, and KNN.

All the models were trained and tested with the dataset from experiment E1 and validated with data from E2. For KNN, Random forest, SVM, and LR, the dataset from E1 was further randomly divided into an 80% training set and a 20% testing set. Results were averaged over four different data splits, and hyperparameter tuning was performed using the grid search approach implemented with the GridSearchCV function (sklearn) using the repeated K-fold cross-validation method. For GLR and GPR, the entire E1 dataset was utilized for training.

The average performances of the tuned ML models on the training dataset are presented in Table I.

TABLE I
COMPARISON OF RH PREDICTION ON THE TRAINING DATA SET: FOR LR, SVM, RF AND KNN, PERFORMANCES ARE CALCULATED OVER 20% OF THE DATASET AND AVERAGED OVER 4 RANDOM SPLITS; FOR GLR AND GLR, PERFORMANCES ARE OVER 100% OF THE DATASET

ML models	MAE (%RH)	MAPE (%)	R^2 (%)	Prediction time (ms)
LR	2.4	5.5	94.1	1
SVM	0.8	1.7	99.1	202
RF	0.7	1.6	99.3	32
KNN	0.6	1.5	99.4	6
Exp fit on freqdiff	1.8	4.1	96.3	1
Exp fit on magdiff	0.8	1.8	99.2	1
GLR	1.1	2.5	98.7	1
GPR	0.5	1.2	99.6	2000

The performances on the validation dataset E2 are displayed in Table II. Figs. 8a-f further illustrate the comparison between the true RH measured by the SHT85 sensor and the predicted RH values on the validation dataset E2. Fig. 9, for instance, compares the time-domain RH prediction of the sensor using the KNN model with the reference RH measured with SHT85.

TABLE II
COMPARISON OF THE CALIBRATION MODELS ON RH PREDICTION FROM THE TEST DATA SET (EXPERIMENT 2)

ML models	MAE (%RH)	MAPE (%)	R^2 (%)	Prediction time (ms)
LR	2.2	5.5	93.8	2
SVM	1.1	2.4	98.6	864
RF	1.0	2.3	98.6	64
KNN	1.0	2.2	98.7	16
Exp fit on freqdiff	1.9	4.4	95.4	1
Exp fit on magdiff	0.8	1.8	99.2	1
GLR	1.1	2.5	98.8	1
GPR	0.9	2.2	99.1	12000

All trained models demonstrate good performance in RH prediction on both the testing (E1) and validation (E2) datasets, with MAE < 2 %RH, MAPE < 6%, and R^2 > 95%. The

performance degradation between E1 and E2 is minimal, indicating the sensor's stability between the two experiments and absence of overfitting.

Moreover, all models, except LR and the exponential fit on the frequency feature, show comparable performances. The non-linearity of the response (Fig. 8a) presents a challenge for LR, while a larger dispersion of the model (Fig. 8e) likely causes the difficulty for the model on frequency.

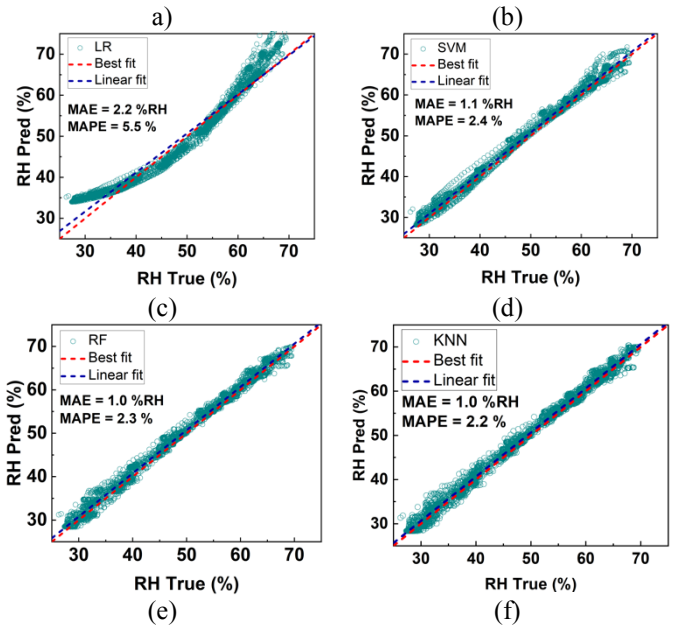

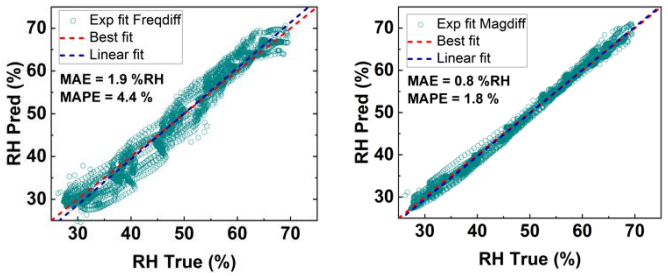

Fig. 8. Scatter plot of true RH% and predicted RH% from the test data based on E2 using (a) LR (b) SVM (c) RF (d) KNN (e) Exp fit on freqdiff and (f) Exp fit on magdiff with their corresponding evaluation metrics (R^2, MAE and prediction time). The red line is the best fit line (predicted RH% = true RH%) and the blue line is the actual linear fit on the data.

The best performance on E1 is achieved by GPR with 0.5 %RH MAE and 1.2 %RH MAPE. On E2, the exponential fit on the differential magnitude response provides the best performance with 0.8 %RH MAE and 1.8 %RH MAPE. These performances are on par with the benchmark humidity sensor's accuracy (±1.5 %RH) as per the datasheet [29].

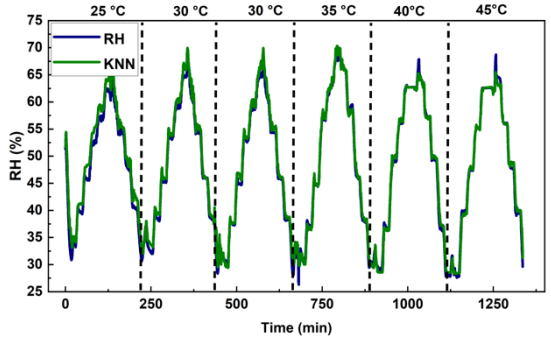

Fig. 9. Time domain comparison of the true RH and KNN prediction of RH from the test data set (experiment 2).

Importantly, despite comparable performances, the models exhibit significant differences in computation times. The exponential fit on magnitude and the GLR are the fastest, followed by KNN. While the exceptional quality of the exponential fit on magnitude allows for analytical calibration in this instance, this is not generally the case for most sensors. The model comparison presented here suggests that using GLR or KNN provides a good balance between prediction quality and computation time when an analytical model is unavailable or underperforms.

IV. Outdoor Sensing Performance Evaluation

This section investigates the adaptability of sensor performance from laboratory-based tests to real-world outdoor scenarios. A second sensor, S2, identical in geometry and sensitivity, was fabricated and briefly calibrated in the lab (during experiment E3) before being deployed at the Sense-City platform for a two-day field study (experiment E4). To gauge the influence of various environmental parameters on the sensor's responses and calibration, we compared outdoor calibration models that each incorporated a different environmental variable, with models that only used RH as an input.

A. Laboratory sensor calibration at room temperature

In experiment E3, the sensor was subjected to a single RH cycle (increase then decrease) from 0 to 90% RH at a standard room temperature of 22°C (refer to Fig. 10a and b).

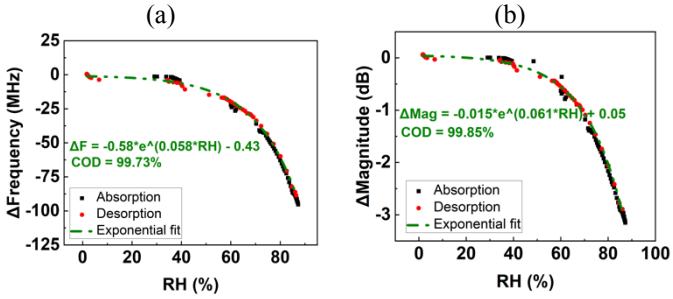

Fig.10. Differential frequency (a) and magnitude (b) response of sensor S2 as a function of relative humidity during experiment E3 in laboratory conditions at room temperature (22°C). The exponential fits and their corresponding coefficients of determination (COD) are provided. The dark and red lines show the increasing and decreasing RH phase respectively. The dash green lines are the exponential fits over the full RH range.

The sensor's responses across this range (0 – 90 %RH) align well with an exponential model, although the coefficients differ from those of sensor S1.

The data from E3 was divided into an 80% training set and a 20% testing set. Results were averaged over four different data splits. The exponential calibration models yield MAE of 5.5 %RH, 10.5 %RH and R^2 of 92 % and 68 % on the magnitude and frequency response respectively.

The coefficients of the calibration equation derived from the whole E3 data set is given in equation (6) and (7).

$$\Delta f\ (\mathrm{MHz}) = -0.58 * e^{(0.058*\mathrm{RH})} - 0.43 \quad (6)$$

$$\Delta \mathrm{Mag}\ (\mathrm{dB}) = -0.015 * e^{(0.061*\mathrm{RH})} + 0.051 \quad (7)$$

B. Sensor outdoor response

The sensor was set up at the Sense-City platform outdoors from 26th to 28th July 2022. Fig. 11a displays the RF sensor's differential responses and the environmental variables recorded by the reference sensors (Envea analyzers and Vaisala WXT536) are presented on Figs. 11b-d.

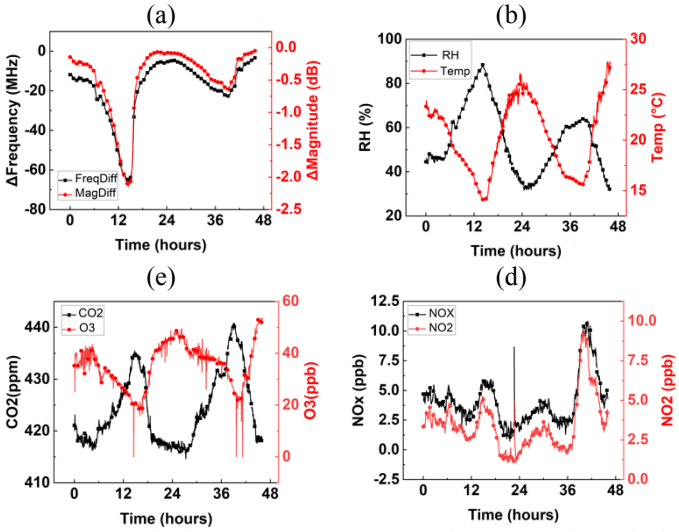

Fig. 11. RF and reference sensors outputs (a) frequency and magnitude response, (b) RH and temperature, (c) CO_2 and O_3, (d) NO_X and NO_2.

Daily cycles are apparent in both the sensor responses and environmental parameters. A strong correlation exists between

the sensor's frequency (freqdiff) and magnitude (magdiff) responses as depicted in the correlation heatmap (Fig. 12).

The strongest correlations with the sensor outputs are seen with humidity and temperature. CO_2 and O_3 exhibit weaker correlations, while NO_x shows no clear correlation. However, considering that RH, temperature, O_3, and CO_2 are highly interrelated in outdoor settings, a correlation between sensor responses and a specific variable does not necessarily indicate sensitivity to that variable. For instance, a correlation with CO_2 could be due to the sensor's sensitivity to humidity and the correlation between CO_2 and humidity.

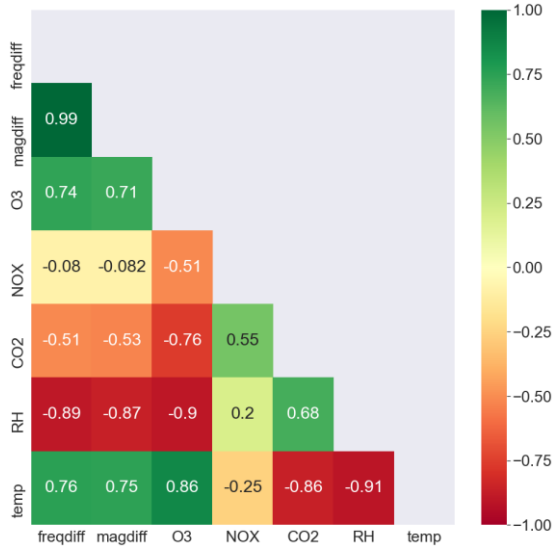

Fig. 12. Correlation heatmap between the sensor outputs (freqdiff, magdiff) and the environmental variables.

C. *Application of the laboratory calibration model to the outdoor dataset*

Figs. 13a and b illustrate the sensor's frequency and magnitude response as a function of outdoor RH and of temperature (color bar). Notably, a significant hysteresis is observed during decreasing RH (80 – 30 %RH) of the first day (12 – 24h). The sensor responses in outdoor settings show exponential variations with RH ($\Delta f\,(\mathrm{MHz}) = -0.61 * e^{(0.053*\mathrm{RH})} - 2.81$ and $\Delta\mathrm{Mag}\,(\mathrm{dB}) = -0.008 * e^{(0.061*\mathrm{RH})} + 0.05$) which are similar to the laboratory results, as indicated by the fit lines in Figs. 13a and b.

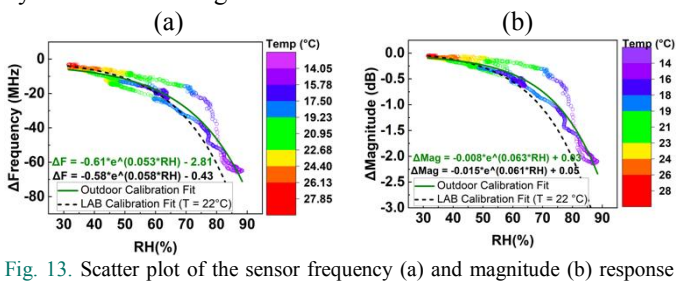

Fig. 13. Scatter plot of the sensor frequency (a) and magnitude (b) response versus outdoor RH and temperature (color bar) over 2 days. The green lines show the exponential fit on the outdoor data and the dash black lines represent the laboratory calibration.

The outdoor RH was predicted using lab data (from experiment E3) via the mathematical calibration relationships outlined in equations (3) and (4), or with LR, generalized linear regression (GLR, 2nd order), or GPR. The results are summarized in Table III.

The best prediction was achieved with the exponential law on frequency, with a Mean Absolute Error (MAE) of 4.2% RH and a R^2 of 88%, which is slightly superior to the lab performance of 3.3% RH MAE. Here, analytical models outperformed machine learning (ML) calibrations due to the limited data set.

D. *Identification of interfering factors*

The performance reported in Table III indicate a minor degradation compared to sensor S1's laboratory performances in E3. To decipher the causes behind this increased error, Fig. 14a presents predicted RH against measured RH using the exponential calibration on frequency.

The most significant errors are represented by a series of points below the diagonal line, marked in red. These points are also depicted in Fig. 14b in relation to time, which evidently correspond to intervals of decreasing RH. This pattern aligns with the hysteresis observed in Fig. 13.

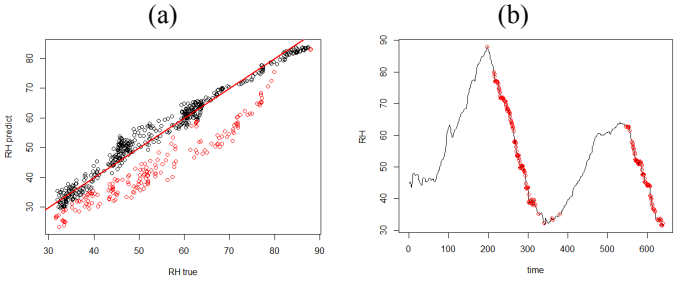

Fig. 14. Calibration based on magnitude: a) predicted RH as a function of measured RH b) Measured and predicted RH as a function of time. Red circles correspond to points with high prediction errors.

To assess whether this hysteresis, and more generally the increased prediction error in outdoor environments, could be attributed to environmental factors, a series of two-variable GLR models were constructed. For this, each one of the environmental parameters was tested as a variable in addition to RH, using a 1:1 split (training over day 1, testing over day 2) of dataset E4. The following models were built: $magnitude = P_1(RH, EV)$ and $frequency = P_2(RH, EV)$, where EV is a second environmental variable among temperature, O_3, CO, CO_2, NO and NO_2 and P_1 and P_2 are two polynomial functions of RH and EV. Subsequently, with RH assumed to be a known quantity, these two models were

TABLE III
COMPARISON OF THE PERFORMANCE OF THE LABORATORY CALIBRATION MODELS ON RH PREDICTION FROM THE OUTDOOR DATASET (EXPERIMENT 4)

Laboratory calibration models	MAE (%RH)	MAPE (%)	R^2 (%)
Exp fit on freqdiff	4.2	8.2	88
Exp fit on magdiff	4.4	8.0	87
GPR	5.6	11	85
LR	6.1	12	75
GLR (order 2)	5.8	10	75

employed to predict the secondary variable EV. The coefficient of determination R^2 for the model $EV_{predicted} = a.EV_{measured} + b$ was then calculated (e.g. R^2 = 100%, a = 1 and b = 0 indicates a perfect prediction).

Table IV shows that accounting for other variables beside RH only yields a minor increase in R^2 value at the calibration stage.

Additionally, during the inversion stage, the negative R^2 values indicate a lack of correlation between the predicted and actual measurements of the environmental variables, implying that the models are not predictive. Taken together, these results suggest that, under outdoor conditions, the sensor's performance is predominantly governed by humidity, with other environmental variables having no discernible impact.

V. Calibration Transfer

The analytical calibration relationships of sensor 1 and sensor 2 (equations 3, 4, 6 and 7) have the same form with different coefficients. This indicates the consistency between the sensors, but also the need for individualized sensor calibration. Proceeding to calibration experiments as extensive as experiments E1 is not feasible for each individual sensor, even at prototype level. As an alternative, once an accurate calibration model (called primary calibration) is available for one of the sensors, calibration transfer allows to fine-tune it for another sensor based on very few additional data points, called transfer standards [30]. We have investigated whether the models developed on experiment E1 for sensor S1 (Fig. 5a) can be applied to sensor S2 experiment E3 (lab data Fig. 9) and experiment E4 (outdoor data, Fig. 13) using calibration transfer algorithms.

In general, calibration transfer uses one of the following approaches: standardization of the sensor's responses (prior to applying the primary calibration), update of the primary calibration model (using the transfer standards as additional datapoints), or standardization of the model outputs (after applying the primary calibration). As a proof of concept, we tested here two classical transfer algorithms, Direct response Standardization (DS), and output standardization by Slope-Bias Correction (SBC).

In DS [30, 31], the transfer matrix $\hat{F}$ is defined as $\hat{F} = \overline{R_2}^{+}\,\overline{R_1}$, where $\bar{X}^{+}$ is the pseudo-inverse of $\bar{X}$, $\overline{R_1}$ denotes the response of sensor 1 (respectively $\overline{R_2}$ for sensor 2). The corrected response of sensor 2 is derived as $R_{2,corr} = R_2\,\hat{F}$. The primary calibration (e.g. model for sensor 1) is then directly applied to $R_{2,corr}$.

By contrast, in SBC [30, 32], writing f_{S1} the primary calibration, one defines $H_1 = f_{s1}(\overline{R_1})$ as its outputs for the transfer standards $\overline{R_1}$. One also defines $H_2 = f_{s1}(\overline{R_2})$ as the outputs of model 1 applied to the transfer standards acquired for sensor 2. Then one estimates α, β, such that $H_1 = \alpha H_2 + \beta$. The corrected response of sensor 2 is then calculated as $H_{2,corr} = \alpha f_{s1}(R_2) + \beta$.

The performances of these two algorithms were applied to sensor S2 experiments E3 and E4 using as primary calibration a KNN model for sensor S1 developed on experiment E1 (LR, RF and SVM calibrations were also tested and gave similar results). The transfer standards of E3 and E4 were selected to be the relative humidity data points exactly equal to the ones of experiment 1: 64 points out of 414 in experiment 3 (15%), 290 out of 1382 in experiment 4 (21%).

Results are presented in Table V: the MAE for sensor S2 achieved with the DS and SBC methods are compared to the MAE values derived from directly applying the primary calibration to S2 (direct transfer), calibrating S2 based only on the transfer standards of E3 and E4 (transfer standard-based calibration), calibrating S2 on the entirety of E3 and E4 (full calibration – the best possible result for S2), and using the naïve model that simply returns the mean of the dataset (R^2 = 0).

The optimal results for E3 are 3.7% RH MAE, while the naïve model provides 28% RH. For E4, it was 3.0%RH MAE and 13% RH for the optimal and the naïve models respectively. Both experiments, direct transfer of S1 model to S2 data, or calibration of S2 only on the transfer standards, improve the results compared to the naïve model, but results remain far from the target. This confirms the need for either S2-specific calibration (with larger amount of data) or for calibration transfer. We observe that SBC and DS algorithms significantly improve MAE compared to direct transfer of S1 model. However, only SBC transfer improves the MAE compared to TS-only calibration (by 22% and 42% in experiment 3 and 4, respectively). While this result validates the added value of calibration transfer for this type of sensors, it underlines the need for careful selection of the transfer algorithms depending on the expected datasets.

TABLE V
COMPARISON OF MAE (EXPRESSED IN %RH) OF SENSOR S2 DEPENDING ON THE CALIBRATION METHOD

Calibration strategy	Algorithm	Exp 3 (lab)	Exp 4 (Sense-City)
Calibration transfer from S1	Direct standardization	15	5.9
	Slope-Bias Correction	14	4.1
	Direct transfer (no correction)	20	11
Direct calibration of S2	Calibration on Transfer standards	18	5.2
	Calibration on all data	3.7	3.0
Naïve model		28	13

VI. Conclusion

A polyethyleneimine polymer-based RF sensor, designed for humidity monitoring, was rigorously tested in both laboratory and field conditions. The sensor demonstrated a range of

TABLE IV
COMPARISON OF PERFORMANCES OF THE GLR MODELS INTEGRATING A SECOND ENVIRONMENTAL VARIABLE (EV) IN ADDITION TO RH.

Variables (RH, EV)	Calibration R^2 Train (%)	Calibration R^2 Test (%)	Inversion EV R^2 (%)
RH	92.9	92.6	
RH, temperature	93.7	92.9	-15
RH, CO_2	94.0	92.4	-2200
RH, O_3	94.7	94.3	-4.6
RH, NO_2	94.9	92.3	-35
RH, CO	95.2	94.6	-210
RH, NO	95.6	94.7	-46

remarkable capabilities, including high sensitivity, quick response/recovery time, repeatability, reversibility, and minimal hysteresis. Calibration models derived from lab data allowed for precise prediction of RH at various temperatures (25 – 45 °C) with low MAE and a high R^2. Furthermore, the sensor's outdoor responses exhibited an exponential relationship to RH, similar to the lab results. This lab-based calibration proved effective for predicting outdoor RH, yielding satisfactory MAE and a high R^2. This confirmed the sensor's suitability for outdoor RH monitoring, and it was observed that other uncontrolled environmental factors such as temperature and the presence of different gases had minimal impact on the sensor's RH sensing performance. However, the limited duration of the outdoor measurements resulted in strong correlations between the environmental variables, complicating the task of distinguishing their individual impacts on the sensor's responses. In future work, longer outdoor deployments of several sensor with different sensing materials will be conducted, and calibration models will be employed in a multioutput approach to enable accurate prediction of both RH and other gases.

Regarding the temperature, several prediction models relying on the introduced ML methods were built to predict it knowing the RH and the sensor outputs. But the inability of all these models to correctly predict it leads us to conclude that the sensor can be considered as not dependent on temperature.

Overall, the sensors demonstrated high performance in RH sensing, with negligible temperature cross-sensitivity, resulting in mean absolute errors (MAE) of 0.8% RH in laboratory conditions and 4.4% RH outdoors.

FUNDING

This work was carried out with the financial support of the Agence Nationale de la Recherche (ANR) for projects CARDIF (ANR-19-CE04-0010) and CAMUS (ANR-13-BS03-0010), of the French region Nouvelle-Aquitaine (project CARGESE, 2017-1R10123), and of project LOTUS, co-funded by both the European Commission under the Horizon 2020 research and innovation program under Grant Agreement N° 820881 and the Indian Government, Ministry of Science and Technology.

ACKNOWLEDGMENT

Authors are grateful for the help of Stéphane Laporte et Yan Ulanowski for the outdoor characterization experiments at Sense-city.

REFERENCES

[1] F. Li, Y. Zheng, C. Hua, and J. Jian, "Gas sensing by microwave transduction: Review of progress and challenges," *Frontiers in Materials*, vol. 6, p. 101, 2019.

[2] H. Hallil *et al.*, "Passive Resonant Sensors: Trends and Future Prospects," *IEEE Sensors Journal*, vol. 21, no. 11, pp. 12618-12632, 2021, doi: 10.1109/jsen.2021.3065734.

[3] B. Wu, X. Zhang, B. Huang, Y. Zhao, C. Cheng, and H. Chen, "High-Performance wireless ammonia gas sensors based on reduced graphene oxide and Nano-Silver ink hybrid material loaded on a patch antenna," *Sensors*, vol. 17, no. 9, p. 2070, 2017.

[4] P. Bahoumina *et al.*, "Microwave flexible gas sensor based on polymer multi wall carbon nanotubes sensitive layer," *Sensors and Actuators B: Chemical*, vol. 249, pp. 708-714, 2017.

[5] N. Wang, N. Zhang, and M. Wang, "Wireless sensors in agriculture and food industry—Recent development and future perspective," *Computers and electronics in agriculture*, vol. 50, no. 1, pp. 1-14, 2006.

[6] B. Arman Kuzubasoglu, "Recent Studies on the Humidity Sensor: A Mini Review," *ACS Applied Electronic Materials*, vol. 4, no. 10, pp. 4797-4807, 2022.

[7] X. Zhang, D. He, Q. Yang, and M. Z. Atashbar, "Rapid, highly sensitive, and highly repeatable printed porous paper humidity sensor," *Chemical Engineering Journal*, vol. 433, p. 133751, 2022.

[8] B. B. Ngoune *et al.*, "Selective Outdoor Humidity Monitoring Using Epoxybutane Polyethyleneimine in a Flexible Microwave Sensor," *Chemosensors*, vol. 11, no. 1, p. 16, 2022.

[9] X. Wang, J.-G. Liang, J.-K. Wu, X.-F. Gu, and N.-Y. Kim, "Microwave detection with various sensitive materials for humidity sensing," *Sensors and Actuators B: Chemical*, vol. 351, p. 130935, 2022.

[10] B. B. Ngoune *et al.*, "Humidity and Temperature Dual Flexible Microwave Sensor," in *2022 29th IEEE International Conference on Electronics, Circuits and Systems (ICECS)*, 2022: IEEE, pp. 1-4.

[11] U. Yaqoob and M. I. Younis, "Chemical gas sensors: Recent developments, challenges, and the potential of machine learning—A review," *Sensors*, vol. 21, no. 8, p. 2877, 2021.

[12] G. Forkuor, O. K. Hounkpatin, G. Welp, and M. Thiel, "High resolution mapping of soil properties using remote sensing variables in south-western Burkina Faso: a comparison of machine learning and multiple linear regression models," *PloS one*, vol. 12, no. 1, p. e0170478, 2017.

[13] G. Perrin and B. Lebental, "Uncertainty-Based Calibration Method for Environmental Sensors—Application to Chlorine and pH Monitoring With Carbon Nanotube Sensor Array," *IEEE Sensors Journal*, vol. 23, no. 5, pp. 5146-5155, 2023.

[14] G. Mountrakis, J. Im, and C. Ogole, "Support vector machines in remote sensing: A review," *ISPRS Journal of Photogrammetry and Remote Sensing*, vol. 66, no. 3, pp. 247-259, 2011.

[15] M. Belgiu and L. Drăguţ, "Random forest in remote sensing: A review of applications and future directions," *ISPRS journal of photogrammetry and remote sensing*, vol. 114, pp. 24-31, 2016.

[16] J. Vitola, F. Pozo, D. A. Tibaduiza, and M. Anaya, "A sensor data fusion system based on k-nearest neighbor pattern classification for structural health monitoring applications," *Sensors*, vol. 17, no. 2, p. 417, 2017.

[17] J. Yu, "A Bayesian inference based two-stage support vector regression framework for soft sensor development in batch bioprocesses," *Computers & Chemical Engineering*, vol. 41, pp. 134-144, 2012.
[18] D. Zhang *et al.*, "Humidity sensing properties and respiratory behavior detection based on chitosan-halloysite nanotubes film coated QCM sensor combined with support vector machine," *Sensors and Actuators B: Chemical*, vol. 374, p. 132824, 2023.
[19] B. Lebental *et al.*, "Water and air quality monitoring with multiparameter chemical sensors Managing non-idealities from lab to field," in *2022 IEEE Sensors*, 2022: IEEE, pp. 01-04.
[20] J. Svacina, "Analysis of multilayer microstrip lines by a conformal mapping method," *IEEE transactions on microwave theory and techniques*, vol. 40, no. 4, pp. 769-772, 1992.
[21] J. Svacina, "A simple quasi-static determination of basic parameters of multilayer microstrip and coplanar waveguide," *IEEE microwave and guided wave letters*, vol. 2, no. 10, pp. 385-387, 1992.
[22] C. Zhu, R. E. Gerald II, and J. Huang, "Highly sensitive open-ended coaxial cable-based microwave resonator for humidity sensing," *Sensors and Actuators A: Physical*, vol. 314, p. 112244, 2020.
[23] W. Qu, W. Wlodarski, and J.-U. Meyer, "Comparative study on micromorphology and humidity sensitive properties of thin-film and thick-film humidity sensors based on semiconducting MnWO4," *Sensors and Actuators B: Chemical*, vol. 64, no. 1-3, pp. 76-82, 2000.
[24] W. ELEKTRONIK. https://www.we-online.com/en (accessed.
[25] DUPONT. "DUPONT™ PYRALUX® AP All-Polyimide Double-Sided Copper-Clad Laminate." https://www.dupont.com/content/dam/dupont/amer/us/en/products/ei-transformation/documents/EI-10124-Pyralux-AP-Data-Sheet.pdf (accessed.
[26] F. Pedregosa *et al.*, "Scikit-learn: Machine learning in Python," *the Journal of machine Learning research*, vol. 12, pp. 2825-2830, 2011.
[27] F. Delaine, B. Lebental, and H. Rivano, "Framework for the simulation of sensor networks aimed at evaluating in situ calibration algorithms," *Sensors*, vol. 20, no. 16, p. 4577, 2020.
[28] W. Yuan, K. Yang, H. Peng, F. Li, and F. Yin, "A flexible VOCs sensor based on a 3D Mxene framework with a high sensing performance," *Journal of Materials Chemistry A*, vol. 6, no. 37, pp. 18116-18124, 2018.
[29] Sensirion. "Datasheet SHT85, Humidity and Temperature Sensor." https://www.mouser.com/catalog/specsheets/Sensirion_10022018_HT_DS_SHT85_V0.9_D1.pdf (accessed 16 May, 2023).
[30] A. Rudnitskaya, A. M. S. Costa, and I. Delgadillo, "Calibration update strategies for an array of potentiometric chemical sensors," *Sensors and Actuators B: Chemical*, vol. 238, pp. 1181-1189, 2017.
[31] J. Fonollosa, L. Fernandez, A. Gutiérrez-Gálvez, R. Huerta, and S. Marco, "Calibration transfer and drift counteraction in chemical sensor arrays using Direct Standardization," *Sensors and Actuators B: Chemical*, vol. 236, pp. 1044-1053, 2016.
[32] R. N. Feudale, N. A. Woody, H. Tan, A. J. Myles, S. D. Brown, and J. Ferré, "Transfer of multivariate calibration models: a review," *Chemometrics and intelligent laboratory systems*, vol. 64, no. 2, pp. 181-192, 2002.

B.B Ngoune received a Bachelor degree in electrical and electronics engineering from University of Buea, Cameroun and a M.S degree in smart sensors, micro and nanotechnology from University of Lorraine, France. He joined University of Bordeaux as a PhD student in 2020 and he is actually working on flexible microwave gas sensors for outdoor gas pollutant monitoring.

M. Dumon graduated from Sorbonne University in applied Mathematics. She joined Gustave Eiffel University in 2022 as a PHD student and she is actually working on calibration methods of innovative sensors for monitoring pollutants in uncontrolled environment.

B. Vignesh received his Bachelor of Engineering degree in Electronics and Instrumentation engineering from National Engineering College, Tamil Nadu, India. He joined Indian Institute of Technology Guwahati, India as a PhD student in 2019 and his thesis focuses on Multiparametric CNT based sensors for water quality monitoring within the framework of the LOTUS project https://www.lotus-india.eu/. As part of his PhD degree, he is currently working in Laboratoire Instrumentation, Modélisation, Simulation et Expérimentation (IMSE) at Université Gustave Eiffel, France.

B.Bondu graduated from Ecole Nationale Supérieure des Mines de Nancy in 2008, with a major in Materials Science and Engineering. He subsequently worked as a process engineer and manager at Oerlikon Solar, X-FAB France and Safran REOSC in the fields of photovoltaics, semiconductor device manufacturing and high-precision optics. He then joined Isorg as R&D team leader in 2020, focusing on printed electronics manufacturing techniques.

S. Subbiah obtained his Bachelor of Engineering (B.E.) degree in Chemical Engineering from Bharathiar University, Coimbatore, India and Master of Technology (M.Tech.) degree in Process Engineering and Design with a minor in Chemical

Engineering from Indian Institute of Technology Delhi, India, where he also completed his Ph.D. in Membrane Science and Engineering with a minor in Chemical Engineering. Currently, he serves as a Professor in the Department of Chemical Engineering at Indian Institute of Technology Guwahati, India. His research interests focus on water and energy management, including modeling and optimization, process design and operation of membrane separation processes, waste and wastewater treatment (WWWT) for process industries, water management for oil and gas upstream, smart water grid, waste-to-energy technologies, and novel desalination technologies.Throughout his career, he has made significant contributions to his field, with 31 patent applications, 4 granted US patents, 71 journal publications, 5 book chapters, 2 industrial magazine articles, and 32 conference papers to his name.

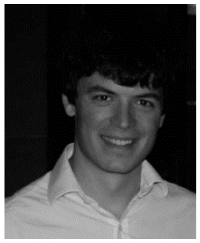

G. Perrin. graduated from Ecole Polytechnique and Ecole Nationale des Ponts et Chausses in 2010. He received the Ph.D. degree in mechanics from University Paris-Est in 2013, and the habilitation to direct research in mathematics from the University Paris-Sud in 2019. From 2013 to 2020, he was a research scientist at CEA (French atomic agency), and since 2020, he has been a research director at Gustave Eiffel University, in the IMSE laboratory of the COSYS department. His research interests include statistical learning, inverse problem solving in statistics and verification and validation approaches for the design and guarantee of systems under uncertainty. His work has been valorized in the framework of several research projects mainly concerning the validation of AI-based systems, the proposal of innovative methods for monitoring, maintaining and optimizing the performance of dynamic mechanical systems.

S. Bila (M'10) was born in Paris, France, in September 1973. In 1999, he received the PhD degree from the University of Limoges, Limoges, France. He then held a post-doctoral position during one year with the French Space Agency (CNES), Toulouse, France. In 2000, he became a researcher at the National Centre for Scientific Research (CNRS) and joined XLIM (formerly IRCOM), Limoges, France. From 2006 to 2015, he led a research team focused on passive microwave circuits, and since 2016, he leads the RF Systems department gathering four research teams and more than 45 researchers, faculty staffs, and engineers, working on microwave circuits, antennas and EMC. In 2012, Stéphane Bila became a scientific representative for the CNRS. He serves as a reviewer for several journals and conferences. In particular, he was in the Editorial Board of the International Journal of RF and Microwave Computer Aided Engineering, in 2014 and 2015, and since 2007, he is a member of the Scientific Committee of the biannual French Microwave Conference (JNM: Journées Nationales Microondes). His research activities concern computer aided techniques for the advanced design of microwave circuits, including filter synthesis, numerical modelling, and optimisation techniques.

C. Dejous. (M'13) received the electronics engineer degree in 1991 from the French "Grande École" ENSEIRB, Bordeaux, France (M.S degree), and the Ph.D. degree in electronics from the University of Bordeaux, France, in 1994. She is Full Professor at Bordeaux INP, France, where she was responsible for the department on Embedded Electronic Systems from 2013 to 2018. She has been leading research at IMS labs in acoustic and other resonant wave-based (bio)chemical microsensors, her research works also include wireless microdevices for health and environment. From 2016 to 2023, she has been in charge of the IMS Labs' transverse topic "Environments". She co-authored over 250 papers, book chapters, and conference proceedings, and co-supervised 35 research projects.

B. Lebental. graduated from Ecole Polytechnique's Engineering Program in 2006, and from Ecole Polytechnique's Physics and Nanotechnology Master of Sciences Programs in 2007. She obtained her Ph.D. in Civil Engineering from University of Paris-Est, France, in 2010, on the topic of Carbon nanotubes sensors for monitoring construction materials. Since 2010, she is researcher at University Gustave Eiffel. Her research focuses on nano-enabled mechanical and chemical sensors for smart cities. Her research ranges from nanosensor design and fabrication to field deployment and data exploitation. She has coordinated several collaborative research projects on sensors for smart cities, such as Sense-City (http://sense-city.ifsttar.fr/) or Proteus (http://www.proteus-sensor.eu/). She is cofounder of the start-up Altaroad (https://www.altaroad.com/en/) which provides traceability solutions for materials in the construction industry.

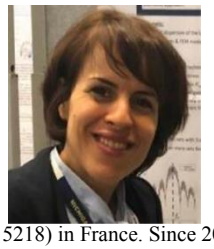

H. Hallil. (M'09) received Ing. and M.S. degrees in electrical engineering from the USTHB University, Algiers, Algeria, and from Institut National Polytechnique de Toulouse, France, in 2005 and 2007 respectively, and the Ph.D. degree in nano and micro systems from Toulouse University, in 2010. Since 2011, she has been an Assoc. Prof. in electrical engineering at the Bordeaux University and affiliated with the laboratory IMS (CNRS, UMR 5218) in France. Since 2018 for 2 years, she was assigned as research scientist at School EEE NTU and CNRS International -NTU-Thales Research Alliance (CINTRA) in Singapore. Her research interests include the design and fabrication of innovative devices and sensors using electromagnetic and elastic waves. She is the co-author of a book appeared in Wiley-IEEE Press in 2020, 3 book chapters, more than 70 publications in top-tier journals and conferences. She is Fellow of the French National council of universities section Electrical engineering and systems since 2015 and Chair of IEEE Sensors Council Educational Activity committee since 2022.